Naval Research Laboratory
Washington, DC 20375-5320

NRL/5670/MR—2022/5

Temperature-Strain Discrimination Using the Brillouin Frequency and Linewidth

MATTHEW J. MURRAY

JOSEPH B. MURRAY

BRANDON REDDING

Optical Techniques Branch
Optical Sciences Division

July 7, 2022

REPORT DOCUMENTATION PAGE

Form Approved
OMB No. 0704-0188

1. REPORT DATE *(DD-MM-YYYY)*	**2. REPORT TYPE**	**3. DATES COVERED** *(From - To)*
07-07-2022	NRL Memorandum Report	01-03-2022 – 06-29-2022

4. TITLE AND SUBTITLE

Temperature-Strain Discrimination using the Brillouin Frequency and Linewidth

5a. CONTRACT NUMBER

5b. GRANT NUMBER

5c. PROGRAM ELEMENT NUMBER

6. AUTHOR(S)

Matthew J. Murray, Joseph B. Murray, and Brandon Redding

5d. PROJECT NUMBER

5e. TASK NUMBER

5f. WORK UNIT NUMBER
6B93

7. PERFORMING ORGANIZATION NAME(S) AND ADDRESS(ES)

Naval Research Laboratory
4555 Overlook Avenue, SW
Washington, DC 20375-5320

8. PERFORMING ORGANIZATION REPORT NUMBER

NRL/5670/MR--2022/5

9. SPONSORING / MONITORING AGENCY NAME(S) AND ADDRESS(ES)

Naval Research Laboratory
4555 Overlook Avenue, SW
Washington, DC 20375-5320

10. SPONSOR / MONITOR'S ACRONYM(S)

11. SPONSOR / MONITOR'S REPORT NUMBER(S)

12. DISTRIBUTION / AVAILABILITY STATEMENT

DISTRIBUTION STATEMENT A: Approved for public release; distribution is unlimited.

13. SUPPLEMENTARY NOTES

14. ABSTRACT

Distributed fiber optic sensors that can measure and discriminate between temperature and strain have many important applications including 3-dimensional shape sensing and structural health monitoring. A Brillouin-based sensor is a promising choice for these applications since the Brillouin frequency and the Brillouin linewidth have different dependencies on the temperature and strain in the fiber. Here, we designed and constructed a Brillouin optical time-domain analysis (BOTDA) system for this purpose using an optical frequency comb. The system extracts the Brillouin frequency and linewidth at each position in the fiber from the measured Brillouin gain spectrum. The temperature and strain can then be recovered at each position along the fiber under test. We show that this approach enables a temperature resolution of 2 oC and a strain resolution of 50 με with a 10 m sensing aperture. Finally, we discuss the limitations of this technique due to non-uniformities within the sensing aperture and provide a comparison with alternative schemes for temperature/strain discrimination.

15. SUBJECT TERMS

Temperature sensing
Fiber optics
Strain sensing
Brillouin Scattering

16. SECURITY CLASSIFICATION OF:			**17. LIMITATION OF ABSTRACT**	**18. NUMBER OF PAGES**	**19a. NAME OF RESPONSIBLE PERSON**
					Matthew J. Murray
a. REPORT	**b. ABSTRACT**	**c. THIS PAGE**	U	16	**19b. TELEPHONE NUMBER** *(include area code)*
U	U	U			(203) 313-6624

Standard Form 298 (Rev. 8-98)
Prescribed by ANSI Std. Z39.18

This page intentionally left blank.

EXECUTIVE SUMMARY

Distributed fiber optic sensors that can measure and discriminate between temperature and strain have many important applications including 3-dimensional shape sensing and structural health monitoring. A Brillouin-based sensor is a promising choice for these applications since the Brillouin frequency and the Brillouin linewidth have different dependencies on the temperature and strain in the fiber. Here, we designed and constructed a Brillouin optical time-domain analysis (BOTDA) system for this purpose using an optical frequency comb. The system extracts the Brillouin frequency and linewidth at each position in the fiber from the measured Brillouin gain spectrum. The temperature and strain can then be recovered at each position along the fiber under test. We show that this approach enables a temperature resolution of 2 ^{o}C and a strain resolution of 50 με with a 10 m sensing aperture. Finally, we discuss the limitations of this technique due to non-uniformities within the sensing aperture and provide a comparison with alternative schemes for temperature/strain discrimination.

This page intentionally left blank.

TEMPERATURE STRAIN DISCRIMINATION USING THE BRILLOUIN FREQUENCY AND LINEWIDTH

Matthew J. Murray, Joseph B. Murray, and Brandon Redding

INTRODUCTION

Background

Distributed fiber optic sensors have been used for a wide variety of applications, from structural health monitoring to perimeter surveillance. These fiber-based systems have several advantages over more conventional sensing mechanisms, including integration into harsh or hard-to-reach environments, immunity to electromagnetic interference, and the ability to make distributed measurements in real time.

Brillouin-based fiber sensors take advantage of light that scatters off of acoustic phonons generated through electrostriction. The scattered light is shifted in frequency from the original light beam by the Brillouin frequency, which depends on the speed of sound in the fiber. The Brillouin frequency is sensitive to both the temperature and strain along the fiber. Traditionally, this dual sensitivity, which can lead to cross-sensitivities in strain or temperature measurements, has been viewed as a disadvantage that must be overcome in Brillouin-based fiber sensors. Yet, there are several applications where the simultaneous measurement of the temperature and strain along a single fiber is both advantageous and necessary. Some of these applications include 3D shape sensing, fire detection, and structural health monitoring. While many Brillouin sensors have achieved remarkable success detecting either strain *or* temperature along the fiber, it is a more challenging problem to simultaneously detect and discriminate between strain *and* temperature along a fiber.

In order to distinguish between temperature and strain it is necessary to have two measurands with different dependencies on temperature and strain. Nearly all Brillouin-based fiber sensors measure the Brillouin frequency (f_{SBS}), which serves as one of the measurands. However, a variety of secondary measurands have been suggested.

Early systems based on Brillouin optical time-domain reflectometry (BOTDR) used the Brillouin frequency shift and the intensity of the spontaneous Brillouin signal (estimated via the Landau-Placzek ratio) as the two measurands [1,2]. These systems achieved a 10m spatial resolution and temperature and strain resolutions of 4ºC and ~300 με, respectively [2]. However, this approach required extensive averaging (~15 minutes) due to the relatively weak spontaneous Brillouin signal.

Later systems used the frequency shift of two or more Brillouin gain peaks [3–7]. These systems use multi-compositional or dispersion-shifted fiber, which have multiple Brillouin gain peaks. The best performing systems were based on a Brillouin optical time-domain analysis (BOTDA) platform, which uses a counter propagating pump and probe beam to stimulate Brillouin scattering. These systems achieved resolutions of 2-4 ºC and 40-80 με [6,7]. However, changes in f_{SBS} with temperature and strain are similar for each of the gain peaks, making discrimination challenging. Additionally, the peaks are often within 200 - 300 MHz of one another, leading to cross talk between the peaks.

Finally, there have been several approaches that combined two distinct sensing mechanisms to discriminate between strain and temperature. One such approach uses a measurement of f_{SBS} and the

Manuscript approved July 6, 2022.

birefringence in polarization maintaining (PM) fiber [8–10]. For example, reference [9] reports an impressive resolution of 0.3 ºC and 12 με using a correlation-domain approach. However, the results were only demonstrated over 8 m of PM fiber and the method used a dynamic Brillouin grating to measure the birefringence, increasing the system complexity. Alternatively, researchers have combined Brillouin sensing with Raman sensing [11] or Rayleigh sensing [12,13]. While the Brillouin-Raman system achieved only modest performance (6 ºC and 150 με), the Brillouin-Rayleigh system achieved competitive resolutions of 1.2 ºC and 15 με. However, these hybrid schemes required multiplexing two independent fiber interrogation systems, increasing the system cost and complexity.

Little research has investigated the use of the Brillouin linewidth along with the Brillouin frequency shift for temperature-strain discrimination. One approach found that in LEAF fiber the Brillouin linewidth decreased with both strain and temperature [14]. They achieved a resolution of 1.8 ºC and 37 με. A similar approach recovered strain and temperature with an artificial neural network [15]. However, the authors did not report the strain or temperature resolution. Nonetheless, this approach is promising due to its simplicity, since it only requires the measurement of a single gain spectrum and could be compatible with most standard BOTDA systems.

In this report, we describe a Brillouin-based sensor that can discriminate between temperature and strain using the Brillouin frequency shift and the Brillouin linewidth. We present a modified BOTDA system that uses an optical frequency comb to measure the Brillouin gain spectrum. This approach exhibits reduced susceptibility to crosstalk and precludes the need for frequency scanning, simplifying the sensor design. Using this system, we first calibrated the temperature and strain response of the Brillouin frequency and linewidth. We then demonstrated temperature/strain discrimination in a 300 m fiber with 10 m spatial resolution, achieving a temperature uncertainty of 2 ºC and a strain uncertainty of 50 με in a 50 ms measurement.

Temperature Strain Discrimination

The objective of this sensor is to measure and discriminate between temperature and strain changes along a fiber. In order to achieve this, it is necessary to make two measurements with different dependencies on temperature and strain. The coupled algebraic equations that describe how the two measurands depend on temperature and strain can be written as

$$\begin{bmatrix} M_i \\ M_j \end{bmatrix} = \boldsymbol{C} \begin{bmatrix} \Delta T \\ \Delta \varepsilon \end{bmatrix} \tag{1}$$

where $M_{i(j)}$ is measurand $i(j)$ and $\boldsymbol{C}$ is a matrix of coefficients

$$\boldsymbol{C} = \begin{bmatrix} C_i^T & C_i^\varepsilon \\ C_j^T & C_j^\varepsilon \end{bmatrix}. \tag{2}$$

There exists a unique solution

$$\begin{bmatrix} \Delta T \\ \Delta \varepsilon \end{bmatrix} = \boldsymbol{C^{-1}} \begin{bmatrix} M_i \\ M_j \end{bmatrix} \tag{3}$$

if and only if $\det \boldsymbol{C} \neq 0$. Or, equivalently:

$$\left| \frac{C_j^T - C_i^T}{C_i^T} - \frac{C_j^\varepsilon - C_i^\varepsilon}{C_i^\varepsilon} \right| \equiv |\xi| \neq 0. \tag{4}$$

In most cases, it isn't possible to directly compare the resolutions of different systems because each system has very different FUT lengths, spatial resolutions, and measurement times. Therefore, to compare between temperature-strain discrimination techniques it is convenient to define a figure of merit, $|\xi|$, which was originally proposed in [6], and is defined in Eq. (4). The figure of merit offers a way to determine how

well-suited a set of measurands is at discriminating between temperature and strain. Table 1 shows the figure of merit for several types of temperature-strain discrimination systems. When the figure of merit is small, small perturbations in the input measurands can lead to large changes in the solution. One way to see this is by looking at the uncertainties in the temperature and strain for given uncertainties in the measurands $(\delta M_{i(j)})$:

$$\delta\Delta T = \frac{1}{|\xi| \cdot \left|C_i^{\varepsilon} C_i^{T}\right|}\sqrt{\left(C_j^{\varepsilon}\,\delta M_i\right)^2 + \left(C_i^{\varepsilon}\,\delta M_j\right)^2},$$
$$\delta\Delta\varepsilon = \frac{1}{|\xi| \cdot \left|C_i^{\varepsilon} C_i^{T}\right|}\sqrt{\left(C_j^{T}\,\delta M_i\right)^2 + \left(C_i^{T}\,\delta M_j\right)^2}. \quad (5)$$

As $|\xi|$ increases, the uncertainties in temperature and strain decrease, facilitating temperature-strain discrimination. Note that this figure of merit represents only discrimination performance and does not predict overall sensor noise performance as different measurands may have very different signal to noise levels.

Table 1 — Temperature-Strain Discrimination Methods

Secondary Measurand	$\|\xi\|$	Reference
Spontaneous Brillouin scattering intensity	36	[2]
2nd Brillouin peak	0.16	[6]
Brillouin linewidth	0.083	[14]
Birefringence	76	[9]
Raman	81	[11]
Rayleigh	1600	[13]
Brillouin linewidth	0.12	This work

In this work, we use changes in the Brillouin frequency shift Δf_{SBS} and the Brillouin linewidth, $\Delta\Gamma_B$, as the two measurands, allowing us to re-write Eq. (1) as:

$$\begin{bmatrix}\Delta f_{SBS} \\ \Delta\Gamma_B\end{bmatrix} = \begin{bmatrix}C_{\Delta f}^{T} & C_{\Delta f}^{\varepsilon} \\ C_{\Delta\Gamma}^{T} & C_{\Delta\Gamma}^{\varepsilon}\end{bmatrix}\begin{bmatrix}\Delta T \\ \Delta\varepsilon\end{bmatrix}. \quad (6)$$

For the coefficients reported in this work, $|\xi| = 0.12$. As shown in Table 1, this is a similar figure of merit to Brillouin systems that measure multiple peaks. However, the figure of merit is considerably smaller than hybrid techniques that combine Brillouin sensing with measurements of birefringence, Raman scattering, or Rayleigh scattering. While these hybrid approaches have the potential to provide better discrimination, they are associated with significantly higher cost and complexity. In this work, we investigated the performance which can be achieved using a relatively simple BOTDA system designed to measure a single gain peak.

EXPERIMENTAL SETUP AND APPROACH

Frequency Comb BOTDA

While most BOTDA systems rely on scanning the frequency of the pump or probe beam, this approach has several known challenges. First, frequency scanning the laser itself (e.g. via current or temperature tuning) is prone to non-linearities and can introduce laser intensity noise. Second, frequency scanning using acousto-optic modulators have limited bandwidth, while electro-optic single-sideband modulators can be limited by the sideband extinction. In addition, these modulation techniques can require high-speed electronics to rapidly sweep the laser frequency. Ideally, the sweeping would be done at speeds matching the round-trip time in the fiber, which can be up to ~100 kHz. Finally, these systems are susceptible to laser relative intensity noise, since fluctuations in the gain due to changes in the pump power can distort the measured gain spectrum.

As an alternative, we investigated an optical frequency comb-based approach in this work. In particular, we replaced the normally single-frequency probe with a frequency comb in order to measure the entire gain spectrum without scanning. The frequency comb can be generated with a single EOM driven by a standard arbitrary waveform generator—potentially enabling a simple and low-cost BOTDA system to be adapted for temperature and strain discrimination.

However, detecting the comb is more challenging, since the gain experienced by each comb tooth needs to be measured separately. While heterodyne detection with a local oscillator could be used to identify the different comb teeth, the demodulation needs to be accomplished within the duration of the pump pulse in order to maintain the spatial resolution of the system. To understand the implications of this constraint, consider a system that uses 100 ns pump pulses to achieve 10 m spatial resolution. To demodulate individual comb teeth within 100 ns, the teeth need to be separated by at least the 10 MHz transform limited bandwidth of the pulse, which would seem to place a lower bound on the comb spacing. Unfortunately, measuring the ~30 MHz wide Brillouin gain spectrum with comb teeth spaced by more than 10 MHz would provide a very poor estimate of the linewidth.

In the past, researchers proposed a technique similar to dual comb spectroscopy which used both a comb of pump pulses and a comb of probe tones to overcome this issue [16]. This allowed each probe tooth to interact with the gain spectrum produced by a corresponding pump pulse. However, this approach introduced significant limitations on the available pump power per comb tooth (limiting the Brillouin gain) and was also susceptible to cross-talk between different gain peaks [16].

In this work, we introduce an alternative approach using a single pump pulse and an “aliased” frequency comb measurement technique. This approach allows us to use a frequency comb of closely spaced tones as the probe and demodulate them without compromising the spatial resolution of the system by monitoring the aliased beat frequency produced by the comb teeth and a local oscillator. The key idea is to resample the measured interference signal at the pulse repetition frequency and demodulate the comb teeth at a series of aliased intermediate frequencies, rather than attempting to demodulate the comb within the pump pulse. This process can be repeated at each position in the fiber by resampling the measured data with a different starting point.

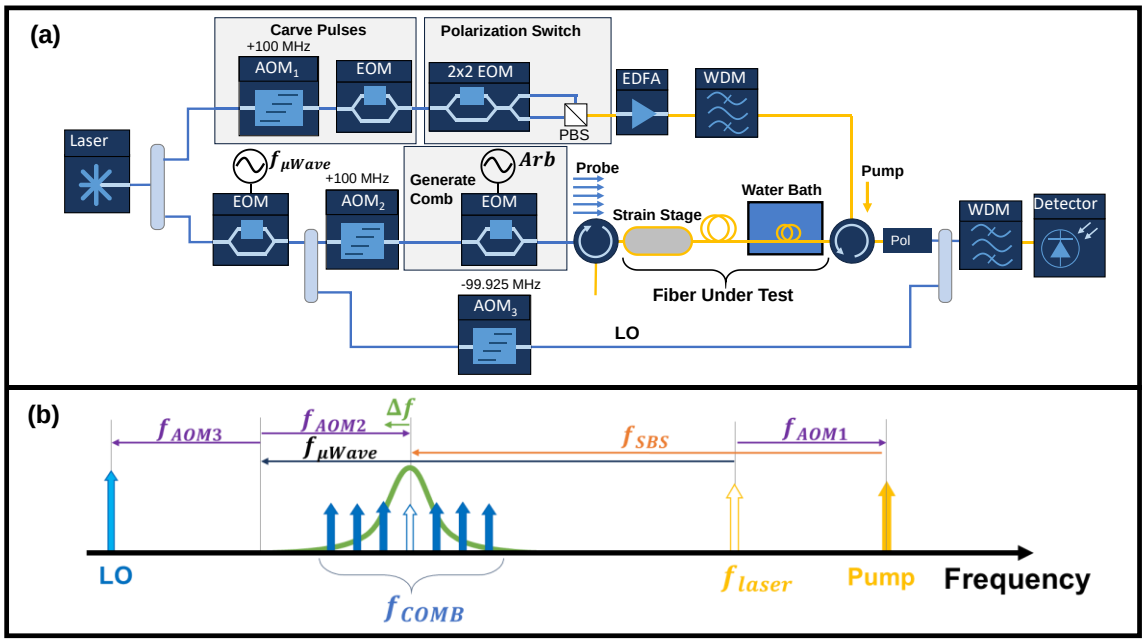

Fig. 1 — (a) Experimental setup of frequency comb BOTDA temperature-strain sensor. The inset in the figure identifies the sections of the fiber under test. (b) Frequency diagram showing the relative frequencies of the comb, LO, and pump beam. Note that in this work, the frequency comb consisted of 21 lines spaced by ~4 MHz.

A schematic of the comb-based BOTDA system used in this work is shown in Fig. 1(a). Light (λ = 1549.73 nm) from a narrow linewidth laser (OE Waves 4028) is split into pump and probe arms. In the upper arm, which served as the Brillouin pump, an acousto-optic modulator (AOM) and electro-optic modulator (EOM) pair was used to carve 100 ns pulses at a 200 kHz repetition rate. The pulses were directed into a 2x2 EOM which directed alternating pump pulses to opposite ports of a polarizing beamsplitter to compensate for polarization fading [17]. The pulses were amplified by an Er-doped fiber amplifier (EDFA) and a wavelength division multiplexer (WDM) was used as a filter to suppress amplified spontaneous emission (ASE). The pulses were then directed into a 300m fiber under test (FUT) using a fiber optic circulator.

In the lower arm, an EOM was driven in the suppressed carrier mode at $f_{\mu Wave} = 10.86$ GHz, which was set to the nominal Brillouin frequency of the FUT. This produced a pair of sidebands shifted by $f_{\mu Wave}$ above and below the original laser frequency (f_{laser}). The light was then split into two arms: a probe arm and an arm that served as a local oscillator (LO). In the probe arm, the light first passed through an AOM to compensate for the frequency shift induced by the AOM in the pump arm. The probe light was then directed to a second EOM which introduced the optical frequency comb. This EOM was driven with a sum of sine waves at 10 different frequencies, separated by approximately 4 MHz. This generated a frequency comb with 21 different frequencies (the upper and lower sideband for each modulation frequency along with the original probe frequency), spread over ~80 MHz. The frequency comb was then coupled into the FUT through a circulator where it interacted with the counter-propagating pump pulse. Fig. 1(b) shows a diagram of the relative optical frequencies of the pump, the probe comb, and the LO.

The FUT contained several sections of fiber and these sections are identified in the inset in Fig. 1(a). Section A contained a 20 m patch cord of SMF-Simplex fiber. Section B was 20 m of SMF-28e+ that was wrapped on a linear strain stage. Section C was a 200 m section of simplex fiber. Section D was a 20 m section of SMF 28e+. Section E was a 20 m section of SMF-28e+ that had been placed in a temperature controlled (0.1 ºC resolution) water bath. Section F was a 20 m patch cord of SMF-Simplex.

The probe light was coupled out of the FUT via a circulator and directed through a polarizer. A polarization control paddle, not shown, was used to maximize transmission of the probe light through the polarizer. The probe light was then combined with the LO (which was separately shifted by -99.925 MHz as required by aliased processing) and directed to a WDM filter which selected the lower sideband generated by the first EOM. The interference signal was detected with an AC-coupled 800 MHz detector (Terahertz Technologies TIA-952) and digitized at 1 GS/s.

Aliased Comb Processing

Each of the optical frequencies in the comb interferes with the LO at intermediate frequencies ranging from ~160 MHz to ~240 MHz. Fig. 2(a) shows the Fourier transform of the measured interference signal (shown in gray). Since the interference frequencies between the LO and the comb are the only frequencies of interest, a filter with a band pass from 150 to 250 MHz was applied to the data. The Fourier transform of the filtered data is shown in Fig. 2(a) in black and each of the interference frequencies of interest (corresponding to the 21 comb teeth) is highlighted in color.

As with most standard time-domain systems, we used time-of-flight to convert the time-dependent data recorded after each pump pulse enters the fiber to position. Since the polarization was rotated between alternating pump pulses, each position along the fiber was sampled with both polarizations at a rate of $f_s =$ 100 kHz. After resampling the data at 100 kHz, we extracted the gain spectrum at each position in the fiber by performing I/Q demodulation at the aliased interference frequency.

To illustrate this, we calculated the Fourier transform of the resampled data at a typical position in the fiber (z=33 m), as shown in Fig. 2(b). This shows that the interference signal from each of the comb teeth were aliased into the available Nyquist bandwidth ($f_s/2 = 50$ kHz). Note that the aliased frequencies shown in Fig. 2(b) were color coded to match the original interference frequencies shown in Fig. 2(a).

To facilitate this processing technique, the exact frequency separation between the comb teeth and the frequency of the LO were chosen such that the aliased interference frequencies produced by the 21 comb teeth were equally spaced across the 50 kHz Nyquist bandwidth. Care was also taken to ensure that the cross terms produced by the comb teeth interfering with each other were equally spaced in between the aliased interference frequencies of interest. To achieve this, we calculated the frequency separation between the comb teeth as:

$$df_{comb} = df_{nominal} - \frac{f_s/2}{N_{comb}} \tag{7}$$

where $df_{nominal} = 4$ MHz is the nominal frequency separation and N_{comb} is the number of comb frequencies. The LO frequency, f_{LO}, defined as the offset between the LO and the center of the comb, was calculated as:

$$f_{LO} = f_{LO-nominal} + f_s/4 \tag{8}$$

where $f_{LO-nominal} = 199.9$ MHz is the nominal LO offset frequency. As shown in Fig. 2(b), the aliased interference frequencies were equally spaced across the available Nyquist bandwidth. Additionally, the system operated in the strong LO regime so that the cross terms produced by interference between the comb teeth were at least 10 dB weaker than the aliased interference frequencies of interest.

After extracting the amplitude of each comb tooth via resampling and demodulation at the aliased interference frequencies, we calculated the Brillouin gain. In particular, the Brillouin gain $G_{SBS}(z, \Delta f_n)$ experienced by the n^{th} comb tooth at a position z was calculated using the measured amplitude, $A_{meas}(z, \Delta f_n)$ at that position, and a reference measurement $A_{ref}(\Delta f_n)$ of the amplitude of a given comb tooth without the pump pulse present:

$$G_{SBS}(z, \Delta f_n) = \ln\left[A_{meas}(z, \Delta f_n)/A_{ref}(\Delta f_n)\right] \quad (9)$$

The reference measurement was obtained during the "dead time" between pulses (after one pump pulse finished passing through the FUT, but before the next pulse entered the FUT). In this work, the measured gain at each position was averaged over ~45 ms. A typical gain spectrum is shown in Fig. 2(c). Again, the colored circles correspond to the frequencies of the individual comb teeth highlighted in Fig. 2(a,b).

Finally, the gain spectrum was fit to a Lorentzian to recover the Brillouin frequency f_{SBS} and linewidth Γ_B:

$$G_{SBS}(\Delta f) = g\frac{(\Gamma_B/2)^2}{\left(\Delta f - \left(f_{SBS} - f_{\mu Wave}\right)\right)^2 + (\Gamma_B/2)^2} \quad (10)$$

where $\Delta f \equiv \left(f_{pump} - f_{comb}\right) - f_{\mu Wave}$ and f_{comb} is the optical frequency of a given comb tooth.

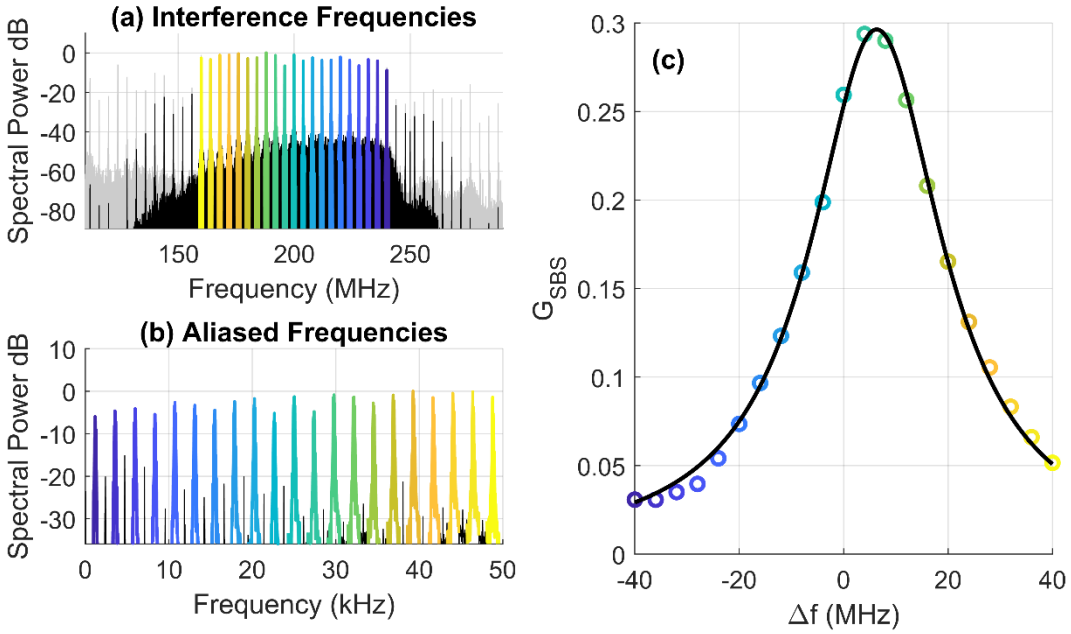

Fig. 2 — (a) Fourier transform of the raw interference signal between the frequency comb and LO (gray) and filtered with a bandpass from 150 – 250 MHz (black). The colors highlight the interference frequencies of interest. (b) Fourier transform of the data at z = 33 m sampled at a rate of 100 kHz. The colors highlight the one-to-one mapping between the original intereference frequencies and the aliased frequencies. (c) The measured Brillouin gain spectrum at z = 33 m. Each colored circle indicates the Brillouin gain measured with an individual comb tooth. The colors highlight the mapping between the interference frequencies, aliased frequencies, and corresponding comb tooth frequencies. The gain spectrum was fit to a Lorentzian function (black).

RESULTS

Position-dependent gain spectra

Fig. 3 (a) shows the measured Brillouin gain at each position along the fiber. For this measurement, the strain stage (section B) was set to 0 με and the water bath (section E) temperature was set to room temperature (~ 25 °C). The various sections of the FUT are identified at the top of the plot and are clearly visible in the shifts in the gain spectrum. In particular, we found that the SMF-Simplex fiber (A, C, and F) has a different Brillouin frequency than the SMF-28e+ (B, D, and E). We also note that the sensor provided the expected 10 m spatial resolution (as measured by the length of the frequency change from one fiber

type to another), confirming that the aliased frequency comb technique maintained the spatial resolution set by the pump pulse.

As described above, we used a Lorentzian fit to extract f_{SBS} and Γ_B at each position in the fiber from the data shown in Fig. 3(a). Fig. 3(b) shows that when f_{SBS} changes rapidly at transitions from one section of fiber to another there are large increases in the measured linewidth. These large increases in the linewidth are not physical, but are an artifact. At the transitions from one section of fiber to another, the 10 m sensing aperture overlaps with both fiber types. Therefore, there are two Brillouin gain peaks at these positions and the fit to a single Lorentzian is artificially broadened. Nevertheless, in the regions where the fiber is uniform over the 10 m sensing aperture the Lorentzian fit provides an accurate measure of the frequency shift and linewidth. Thus, this technique relies on the assumption that the strain or temperature is uniform over the sensing aperture, which is common to many distributed fiber optic sensors.

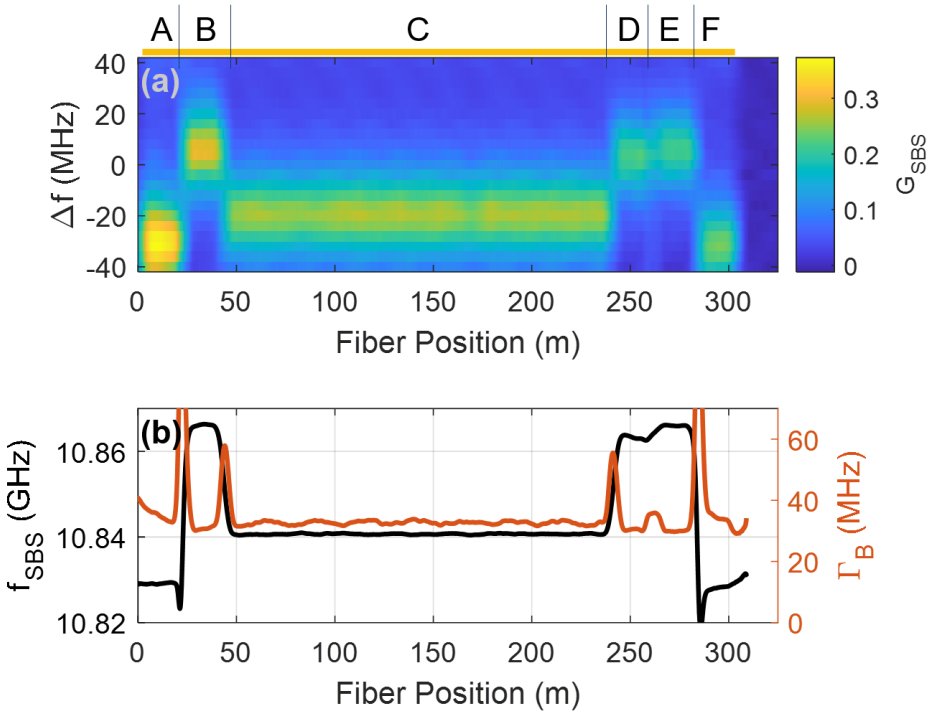

Fig. 3 — (a) Plot of the Brillouin gain G_{SBS} measured at each comb frequency and position along the fiber. The various sections of the FUT are identified at the top of the plot. (b) The Brillouin gain profiles shown in (a) are fit to Lorentzian profiles and the resulting measure of the Brillouin frequency (left axis) and Brillouin linewidth (right axis) is shown as a function of distance.

Calibration experiments

We conducted two calibration experiments in order to determine the coefficients of the matrix in Eq. (5). In the first experiment, the Brillouin gain spectrum was measured all along the FUT as the strain as the strain stage was increased by 368 με in 8 steps. Measurements at each strain level were collected in triplicate. Figs. 4(a) and (b) shows the recovered values of f_{SBS} and Γ_B at the strain stage location (z = 23 – 43 m). Each data point represents a spatial average over a 10 m (equivalent to the sensing aperture) region entirely within the 20 m strained region. A linear regression yielded strain coefficients $C_{\Delta f}^{\varepsilon} = 38 \pm 1$ kHz/με and $C_{\Delta\Gamma}^{\varepsilon} = 0.2 \pm 0.8$ kHz/με. Since $C_{\Delta\Gamma}^{\varepsilon}$ is within the experimental uncertainty, we find that Γ_B is independent of strain, in agreement with several other studies [18–20].

In the second experiment, the temperature controlled water bath was increased from 26 °C to 34 °C in steps of 1 °C. As with the strain measurements, the measurements at each temperature were collected in triplicate. Figs. 4(c) and 4(d) show the recovered values for f_{SBS} and Γ_B at each temperature at the water bath location (z = 263 – 283 m). Again the data points are an average over a 10 m region entirely within

the heated region. A linear regression yielded $C_{\Delta f}^{T} = 1043 \pm 17$ kHz/ºC and $C_{\Delta \Gamma}^{T} = -120 \pm 30$ kHz/ºC. Table 2 summarizes the results from the calibration experiments. These coefficients were used to recover the strain and temperature along the FUT using Eq. (3). Note that the coefficients are in reasonable agreement with values reported in the literature [4,14,18–21]. However, since these coefficients can vary with the exact fiber type and composition, it was important to make our own calibration [4,14,18–21]. The reported coefficients correspond to a figure of merit of $|\xi| = 0.12$, calculated using Eq. (4).

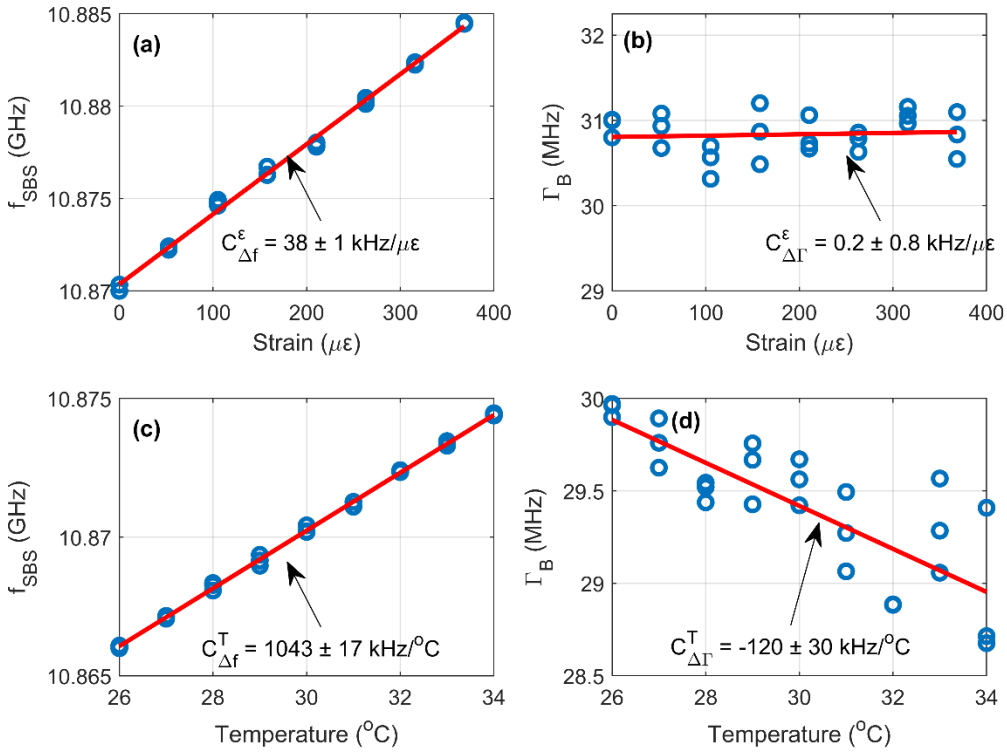

Fig. 4 — Plots showing f_{SBS} (a) and Γ_B (b) measured at the strain stage location as the strain on the fiber was increased by 368 με in 8 steps. Plots showing f_{SBS} (c) and Γ_B (d) measured at the water bath location as the temperature was increased from 26 ºC to 34 ºC. Each data point represents a spatial average over a 10m region within the strained or heated region. Also shown on the plots is a linear regression in red.

Table 2 — Summary of Strain and Temperature Coefficients

Temperature Coefficients		Strain Coefficients	
$C_{\Delta f}^{T}$	1043 ± 17 kHz/ ºC	$C_{\Delta f}^{\varepsilon}$	38 ± 1 kHz/με
$C_{\Delta \Gamma}^{T}$	-120 ± 30 kHz/ ºC	$C_{\Delta \Gamma}^{\varepsilon}$	0.2 ± 0.8 kHz/με

Recovered strain and temperature

In order to evaluate the ability of the sensor to discriminate between temperature and strain we used Eq. (3) and the strain coefficients in Table 2 to recover the strain and temperature at each position along the FUT. For this test we used the same data used to calibrate the sensor and therefore the actual temperature and strain were known at each location. The results were averaged over the 3 repeated measurements. Fig. 5(a) shows the recovered temperature and strain at the strain stage location as the strain was increased. The data show that the strain matches the actual strain and the temperature, which was unchanged, remains fixed. Fig. 5(b) shows the measured temperature and strain at the water bath location as the temperature of the water bath increased. The results show that we correctly recover the strain and temperature at this

location. The data in Figs. 5(a) and 5(b) confirms that the system can discriminate between temperature and strain.

Since the actual strain and temperature is known for each data point in Figs 5(a) and 5(b), the error in the recovered temperature and strain can be used to determine the system's temperature and strain resolutions. We report a temperature resolution of 2 ^{o}C and a strain resolution of 50 $\mu\varepsilon$.

Fig 5(c) shows the recovered change in strain near the strain stage location at 3 different strain levels. The displayed data was averaged over the 3 repeated measurements at each strain level. The plots show that we correctly estimate the strain at the strain stage location. However, at the transition points from the strained region to the unstrained region, there is a large increase in the recovered strain. These locations correspond to the locations where there is a junction between two fiber types (see Fig. 3(a)), which causes the measurement of Γ_B to be artificially enlarged (see Fig. 3(b)). At these transition locations the measurement of Γ_B is not valid and the recovered values of strain and temperature at these locations should be ignored.

Fig. 5(d) shows the average recovered change in temperature as a function of position near the temperature-controlled water bath. The position-dependent data is shown at 3 different temperatures (T = 27 ^{o}C, 31 ^{o}C, and 34 ^{o}C). There is some fluctuation in the temperature within the water bath location due to uneven heating. Similar to the strain measurements, the measured linewidth was corrupted at the transition points where the sensor aperture covered multiple fiber types.

Fig. 5(e) shows the recovered temperature change at the strain stage and Fig. 5(f) shows the recovered strain at the water bath position. We would expect both of these plot to be flat since the temperature was unchanged at the strain stage and the strain was unchanged at the water bath. Figs. 5(c) – 5(f) confirm that the sensor was able to successfully discriminate between temperature and strain in uniform sections of the fiber.

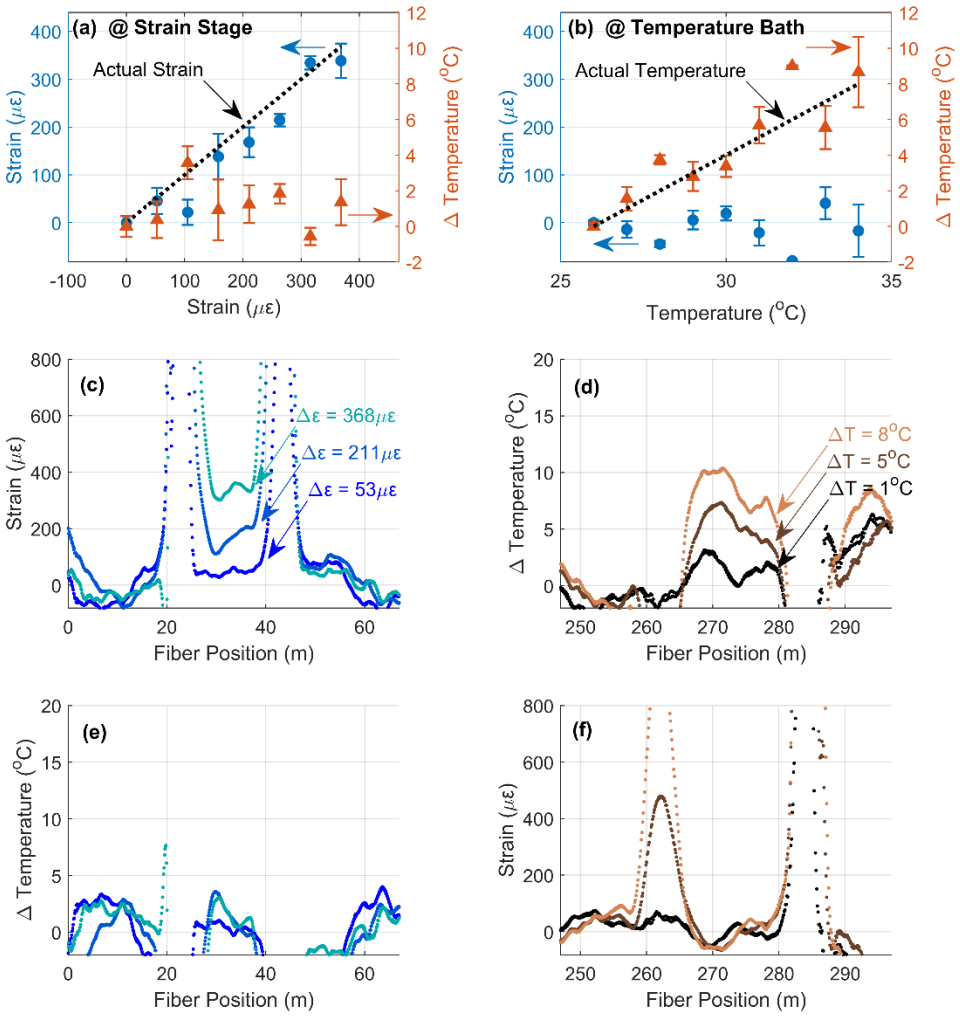

Fig. 5 — Recovered strain (left axis) and temperature (right axis) at the strain stage location (a) and at the temperature-controlled water bath (b). (c) Recovered strain as a function of position near the strain stage at 3 different strain levels. (d) Recovered temperature near the temperature-controlled water bath at 3 different temperatures. (e) Recovered temperature near the strain stage at the same 3 strain levels shown in (c) confirming that the measured temperature is independent of strain. (f) Recovered strain near the water bath at the same 3 temperatures shown in (d) confirming that the measured strain is independent of temperature.

CONCLUSION AND DISCUSSION

Temperature/strain discrimination in distributed fiber optic sensors is a long-standing challenge. Here, we have investigated a simple approach that discriminates between temperature and strain in standard off-the-shelf fiber using a single measurement of the Brillouin gain spectrum. The system is based on a modified BOTDA architecture that uses a frequency comb to measure the Brillouin gain spectrum. We showed that extracting the amplitude of each comb tooth using the aliased intermediate frequencies provides a robust approach to measure the gain spectrum without impacting the spatial resolution of the sensor. We fit the gain spectra to Lorentzians to recover f_{SBS} and Γ_B and used Eq.(3) to extract temperature and strain along the FUT. We report a temperature resolution of 2 ºC and a strain resolution of 50 με, which is comparable to other temperature-strain systems in the literature.

A fundamental limit to the system presented here is the fact that the measured value for Γ_B is artificially enlarged if f_{SBS} is not uniform across the sensing aperture (i.e. due to transitions between fiber-types or rapid variations in strain or temperature). One might consider fitting the measured gain spectrum to multiple Lorentzians at these locations, but since the peaks are often close together and partially overlapping, preliminary analysis suggests that there will still be significant fluctuations and uncertainty in Γ_B at these transition points. Moreover, the FUT investigated in this work was composed of two different types of fiber with distinctly different Brillouin frequencies, exacerbating this issue. Using a FUT composed of a single fiber type could partially mitigate this effect. Alternatively, the data at these positions could be omitted as was suggested in an earlier study using the linewidth [14].

REFERENCES

1. T. R. Parker, M. Farhadiroushan, R. Feced, V. A. Handerek, and A. J. Rogers, "Simultaneous distributed measurement of strain and temperature from noise-initiated Brillouin scattering in optical fibers," IEEE J. Quantum Electron. **34**(4), 645–659 (1998).
2. H. H. Kee, G. P. Lees, and T. P. Newson, "All-fiber system for simultaneous interrogation of distributed strain and temperature sensing by spontaneous Brillouin scattering," Opt. Lett. **25**(10), 695 (2000).
3. C. C. Lee, P. W. Chiang, and S. Chi, "Utilization of a dispersion-shifted fiber for simultaneous measurement of distributed strain and temperature through Brillouin frequency shift," IEEE Photonics Technol. Lett. **13**(10), 1094–1096 (2001).
4. M. Alahbabi, Y. T. Cho, and T. P. Newson, "Comparison of the methods for discriminating temperature and strain in spontaneous Brillouin-based distributed sensors," Opt. Lett. **29**(1), 26 (2004).
5. L. Zou, X. Bao, S. A. V., and L. Chen, "Dependence of the Brillouin frequency shift on strain and temperature in a photonic crystal fiber," Opt. Lett. **29**(13), 1485–1487 (2004).
6. W. Zou, Z. He, M. Kishi, and K. Hotate, "Stimulated Brillouin scattering and its dependences on temperature and strain in a high-delta optical fiber with F-doped depressed inner-cladding," Opt. Lett. **32**(6), 600–602 (2007).
7. Z. Li, L. Yan, X. Zhang, and W. Pan, "Temperature and Strain Discrimination in BOTDA Fiber Sensor by Utilizing Dispersion Compensating Fiber," IEEE Sens. J. **18**(17), 7100–7105 (2018).
8. W. Zou, Z. He, and K. Hotate, "Complete discrimination of strain and temperature using Brillouin frequency shift and birefringence in a polarization-maintaining fiber," Opt. Express **17**(3), 1248 (2009).
9. W. Zou, Z. He, and K. Hotate, "Demonstration of Brillouin Distributed Discrimination of Strain and Temperature Using a Polarization-Maintaining Optical Fiber," IEEE Photonics Technol. Lett. **22**(8), 526–528 (2010).
10. Y. Dong, L. Chen, and X. Bao, "High-spatial-resolution time-domain simultaneous strain and temperature sensor using brillouin scattering and birefringence in a polarization- maintaining fiber," IEEE Photonics Technol. Lett. **22**(18), 1364–1366 (2010).
11. M. N. Alahbabi, Y. T. Cho, and T. P. Newson, "Simultaneous temperature and strain measurement with combined spontaneous Raman and Brillouin scattering," Opt. Lett. **30**(11), 1276 (2005).
12. K. Kishida, C. H. Li, K. Nishiguchi, Y. Yamauchi, A. Guzik, and T. Tsuda, "Hybrid Brillouin-Rayleigh distributed sensing system," in *OFS2012 22nd International Conference on Optical Fiber Sensors* (2012), **8421**(October 2012), p. 84212G.
13. D. P. Zhou, W. Li, L. Chen, and X. Bao, "Distributed temperature and strain discrimination with stimulated brillouin scattering and rayleigh backscatter in an optical fiber," Sensors **13**(2), 1836–1845 (2013).
14. X. Liu and X. Bao, "Brillouin spectrum in LEAF and simultaneous temperature and strain measurement," J. Light. Technol. **30**(8), 1053–1059 (2012).
15. R. Ruiz-Lombera, A. Fuentes, L. Rodriguez-Cobo, J. M. Lopez-Higuera, and J. Mirapeix,

"Simultaneous temperature and strain discrimination in a conventional BOTDA via artificial neural networks," J. Light. Technol. **36**(11), 2114–2121 (2018).

16. A. Voskoboinik, O. F. Yilmaz, A. W. Willner, and M. Tur, "Sweep-free distributed Brillouin time-domain analyzer (SF-BOTDA).," Opt. Express **19**(26), B842-7 (2011).
17. K. Hotate, K. Abe, and K. Y. Song, "Suppression of signal fluctuation in Brillouin optical correlation domain analysis system using polarization diversity scheme," IEEE Photonics Technol. Lett. **18**(24), 2653–2655 (2006).
18. M. Niklès, L. Thévenaz, and P. A. Robert, "Brillouin gain spectrum characterization in single-mode optical fibers," J. Light. Technol. **15**(10), 1842–1851 (1997).
19. S. Le Floch and P. Cambon, "Study of Brillouin gain spectrum in standard single-mode optical fiber at low temperatures (1.4-370 K) and high hydrostatic pressures (1-250 bars)," Opt. Commun. **219**(1–6), 395–410 (2003).
20. K. Brown, A. W. Brown, and B. G. Colpitts, "Characterization of optical fibers for optimization of a Brillouin scattering based fiber optic sensor," Opt. Fiber Technol. **11**(2), 131–145 (2005).
21. W. Zou, Z. He, and K. Hotate, "Investigation of strain- and temperature-dependences of Brillouin frequency shifts in GeO2-doped optical fibers," J. Light. Technol. **26**(13), 1854–1861 (2008).